Article

2D MOF Periodontitis Photodynamic Ion Therapy

Jun Li, Shuang Song, Jiashen Meng, Lei Tan, Xiangmei Liu,* Yufeng Zheng, Zhaoyang Li, Kelvin Wai Kwok Yeung, Zhenduo Cui, Yanqin Liang, Shengli Zhu, Xingcai Zhang,* and Shuilin Wu*

Read Online

ACCESS | 📊 Metrics & More | 📄 Article Recommendations | 🆘 Supporting Information

ABSTRACT: Traditional surgical intervention and antibiotic treatment are poor and even invalid for chronic diseases including periodontitis induced by diverse oral pathogens, which often causes progressive destruction of tissues, even tooth loss, and systemic diseases. Herein, an ointment comprising atomic-layer Fe_2O_3-modified two-dimensional porphyrinic metal−organic framework (2D MOF) nanosheets is designed by incorporating a polyethylene glycol matrix. After the atomic layer deposition surface engineering, the enhanced photocatalytic activity of the 2D MOF heterointerface results from lower adsorption energy and more charge transfer amounts due to the synergistic effect of metal−linker bridging units, abundant active sites, and an excellent light-harvesting network. This biocompatible and biodegradable 2D MOF-based heterostructure exhibits broad-spectrum antimicrobial activity ($99.87 \pm 0.09\%$, $99.57 \pm 0.21\%$, and $99.03 \pm 0.24\%$) against diverse oral pathogens (*Porphyromonas gingivalis*, *Fusobacterium nucleatum*, and *Staphylococcus aureus*) by the synergistic effect of reactive oxygen species and released ions. This photodynamic ion therapy exhibits a superior therapeutic effect to the reported clinical periodontitis treatment owing to rapid antibacterial activity, alleviative inflammation, and improved angiogenesis.
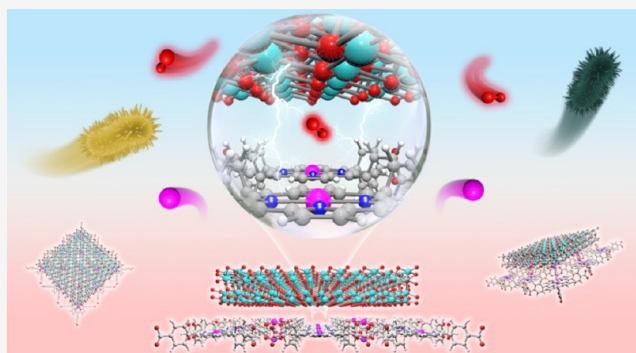
INTRODUCTION

Epidemiologically, periodontitis is one of the most widely prevalent chronic diseases worldwide, and the prevalence increases with age.[1,2] For instance, approximately 50% of US adults aged ≥30 years suffer from periodontitis.[2] Notably, periodontitis originates from diverse oral pathogenic microorganisms, for example, *Porphyromonas gingivalis* (*P. gingivalis*), *Fusobacterium nucleatum* (*F. nucleatum*), and *Staphylococcus aureus* (*S. aureus*).[3−6] Furthermore, chronic periodontitis accompanied by excess inflammatory response induces progressive destruction of tooth-supporting tissues (including gingiva, periodontal ligament, and alveolar bone).[1,4] If patients do not receive appropriate treatment, severe periodontitis may lead to tooth loss and even induce other systemic diseases.[1,7]

Clinically, surgical intervention by mechanical debridement techniques (such as scaling and root planing) with the assistance of local antibiotics therapy in deep periodontal pockets is employed to eradicate periodontal bacteria.[8] However, the current clinical therapy for patients has time-consuming, high-cost, and high-recurrence disadvantages. Meanwhile, the mechanical intervention hinders periodontal tissue regeneration. Besides, the antibiotic therapy (including new generations of antibiotics) usually exhibits inevitable shortcomings, such as narrow-spectrum antibacterial activity, drug-resistant development, and failure of bacterial biofilm. Therefore, a nonsurgical and antibiotic-free therapeutic strategy to rapidly eradicate oral pathogens and effectively accelerate periodontal tissue repair is urgently needed for treating periodontitis.

Currently, photodynamic therapy (PDT) has been applied for treating various diseases in clinical practice, especially in anticancer and antibacterial applications.[9−11] Hence, PDT is expected to be a potential alternative to current clinical therapy for periodontitis. The localized reactive oxygen species (ROS) in target lesions can rapidly kill bacteria using clinically approved photosensitizers, including porphyrins and their derivatives.[12,13] However, the PDT efficiency of porphyrins is limited due to molecular aggregation by planar stacking in aqueous media and a lower absorption coefficient in red light regions of the absorption spectrum.[14]

Metal−organic frameworks (MOFs) have crystalline porous structures by controllable and ordered coordination of metal nodes and organic linkers.[15−20] Numerous studies on MOFs for biomedical applications have been reported recently due to their controllable porous structures and excellent biocompatibility, including phototherapies and nanocarriers for drug loading.[15−20] Thus, porphyrin-based MOFs may achieve
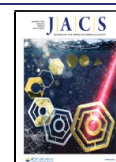
optimized photonic functionality and light-harvesting ability of porphyrins due to the synergistic effect of metal−linker bridging units. Besides, 2D nanosheets have the advantage of abundant active sites, excellent light-harvesting network, and fast energy migration due to a relatively large surface area.[21−24] Therefore, a 2D porphyrinic MOF can be an ideal PDT candidate for treating various clinical diseases including periodontitis. Nevertheless, the limited efficiency of charge transfer and separation also limits the photocatalytic activity.[24,25] Surface engineering may provide an effective strategy to optimize the photocatalytic activity of 2D MOFs. Among them, the atomic layer deposition (ALD) method has great advantages of accurate thickness control and outstanding atomic-scale uniformity due to self-limiting and saturated surface reactions during the process of gas-phase deposition.[26] Therefore, surface-engineered 2D MOFs by ALD are expected to exhibit superior photocatalytic properties. Also, iron(III) oxide nanoarchitectures showed a particular ability of light absorption and separation of photoexcited charges,[27] so atomic-layer Fe_2O_3 prepared by ALD may be promising for surface engineering of 2D MOFs. Moreover, nanostructured Fe_2O_3 with excellent biocompatibility has been approved by the U.S. Food and Drug Administration.[27]

Therefore, we designed an atomic-layer Fe_2O_3-modified 2D porphyrinic MOF (CuTCPP) system (CuTCPP-Fe_2O_3) by ALD, which was incorporated into a polyethylene glycol matrix to form a photoresponsive ointment. Chemically, this strategy can inspire a universal synthetic method by ALD-engineered MOFs to optimize the functionality of MOFs. As schematically illustrated in Scheme 1, the theoretical calculation reveals the

Scheme 1. Schematic Illustration of Engineering a 2D MOF Heterojunction-Based Ointment for Effectively Treating Periodontitis by Photodynamic Ion Therapy
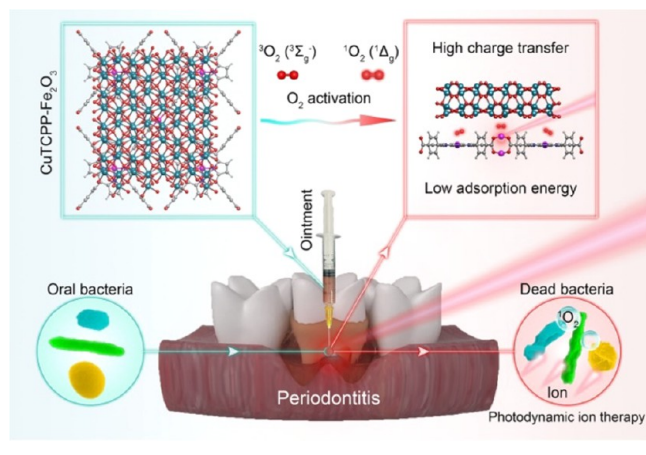
mechanism of enhanced photodynamic activity at the heterointerface by energy evolution pathways and charge transfer, which endows this surface-engineered 2D MOF heterojunction with broad-spectrum antimicrobial activity against diverse oral pathogens through the synergistic effects of ROS and released ions.[27−29] From the biotechnological perspective, this photodynamic ion therapy exhibited a better therapeutic effect than the reported clinical therapy for periodontitis due to alleviative inflammation and promoted angiogenesis. This work may provide a potential alternative to current clinical therapy for diseases like periodontitis through photodynamic ion therapy.

RESULTS AND DISCUSSION

Morphological Characterization. As shown in Figure 1A, CuTCPP nanosheets before sonication had a relatively large lateral size of more than 1 μm, which was observed by transmission electron microscopy (TEM). The experimental procedures of ALD and probe sonication are schematically illustrated in Figure 1B. Briefly, CuTCPP nanosheets prepared by the hydrothermal method were employed to deposit atomic-layer Fe_2O_3 by ALD to obtain CuTCPP-Fe_2O_3 nanosheets. Then, the prepared CuTCPP and CuTCPP-Fe_2O_3 nanosheets were separately disassembled into smaller nanosheets by the mechanical force of probe sonication. The smaller CuTCPP nanosheets (TEM image in Figure 1C) by sonication had an average thickness of ∼6.5 nm measured by atomic force microscopy (AFM) in Figure 1D. The CuTCPP-Fe_2O_3 nanosheets before sonication (TEM image in Figure 1E) had similar lateral sizes to the CuTCPP nanosheets in Figure 1A. Correspondingly, the CuTCPP-Fe_2O_3 nanosheets (TEM image in Figure 1F) after sonication had an average thickness of ∼8.5 nm (AFM image in Figure 1G), which was ∼2 nm thicker than the CuTCPP nanosheets in Figure 1D. Notably, the high-resolution TEM (HRTEM) image of the CuTCPP-Fe_2O_3 in Figure S1A exhibited a lattice distance of 0.253 nm, which belonged to the (110) lattice plane of hematite (α-Fe_2O_3). Correspondingly, the theoretical inter-planar distance (0.253 nm) corresponding to the (110) lattice plane of α-Fe_2O_3 in the crystal structure of CuTCPP-Fe_2O_3 (Figure S1B) was also labeled. Further, the dark-field TEM image and the corresponding elemental mapping images of CuTCPP-Fe_2O_3 nanosheets in Figure 1H obviously displayed a uniform distribution of individual elements of Cu, Fe, C, N, and O, preliminarily confirming the uniform deposition of Fe_2O_3 into CuTCPP. To sum up, ALD to obtain atomic-layer Fe_2O_3 had the advantages of accurate thickness control and outstanding atomic-scale uniformity due to self-limiting and saturated surface reactions during the process of gas-phase deposition.

Structural Characterization. In Figure 1I, X-ray diffraction (XRD) was used to characterize the crystalline structure of the CuTCPP and CuTCPP-Fe_2O_3. The XRD patterns showed three typical peaks indexed as (110), (002), and (004), which could be ascribed to the tetragonal structure of the CuTCPP MOF.[30] Moreover, a broad peak corresponding to the (004) plane demonstrated that the CuTCPP MOF nanosheets with ultrathin crystal nature were preferred in [001] orientation on the solid substrate.[30] In addition, the Raman spectra (Figure 1J) of the CuTCPP and CuTCPP-Fe_2O_3 nanosheets contain all the characteristic Raman peaks of the CuTCPP MOF in the range of 950−1700 cm^{-1}.[31] Specifically, the distinct bands at 993, 1071, 1228, 1356, 1491, 1524, and 1554 cm^{-1} were ascribed to the A_{1g} porphyrin core in-plane mode.[31] Moreover, the characteristic modes at 1177 and 1573 cm^{-1} were assigned to the B_{1g} phenyl ring in-plane mode. Notably, the positions of many characteristic peaks of CuTCPP-Fe_2O_3 slightly shifted into the lower direction when compared with those of CuTCPP, indicating the existence of an interaction between CuTCPP and Fe_2O_3. Besides, the disappearance of the 1573 cm^{-1} band of CuTCPP-Fe_2O_3 further confirmed the formation of an interfacial interaction between CuTCPP and Fe_2O_3.

The Fourier transform infrared spectrometer (FTIR) spectra (in Figure S2) revealed that the peak characteristics of
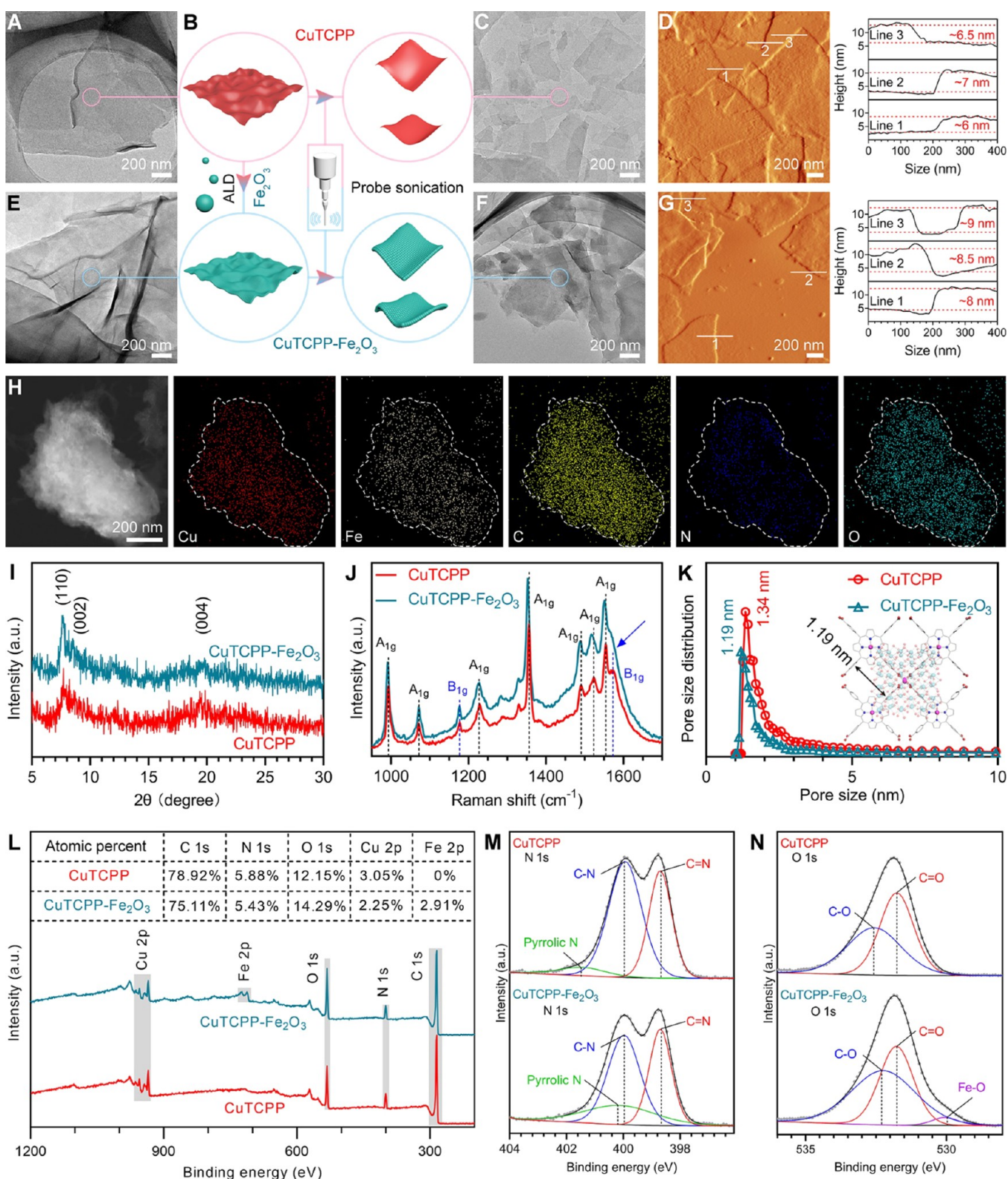
Figure 1. Morphological and structural characterization. (A) TEM image of CuTCPP nanosheets before sonication. (B) Schematic illustration of the synthesis of CuTCPP-Fe$_2$O$_3$ nanosheets. (C) TEM image. (D) AFM image and corresponding height profiles of CuTCPP nanosheets after sonication. (E) TEM image of CuTCPP-Fe$_2$O$_3$ nanosheets before sonication. (F) TEM image. (G) AFM image and corresponding height profiles of CuTCPP-Fe$_2$O$_3$ nanosheets after sonication. (H) Dark-field TEM image and corresponding elemental mapping images (Cu, Fe, C, N, O) of CuTCPP-Fe$_2$O$_3$ nanosheets. (I) XRD patterns. (J) Raman spectra. (K) Pore-size distribution curves of CuTCPP and CuTCPP-Fe$_2$O$_3$. (L) Survey, (M) N 1s, and (N) O 1s of XPS spectra of CuTCPP and CuTCPP-Fe$_2$O$_3$.

CuTCPP and CuTCPP-Fe$_2$O$_3$ mainly corresponded to those of TCPP. Specifically, the peaks near 2950 cm^{-1} were ascribed

to C−H stretching vibrations in the aromatic ring. The peaks around 1600 and 1660 cm^{-1} were caused by the C═O and
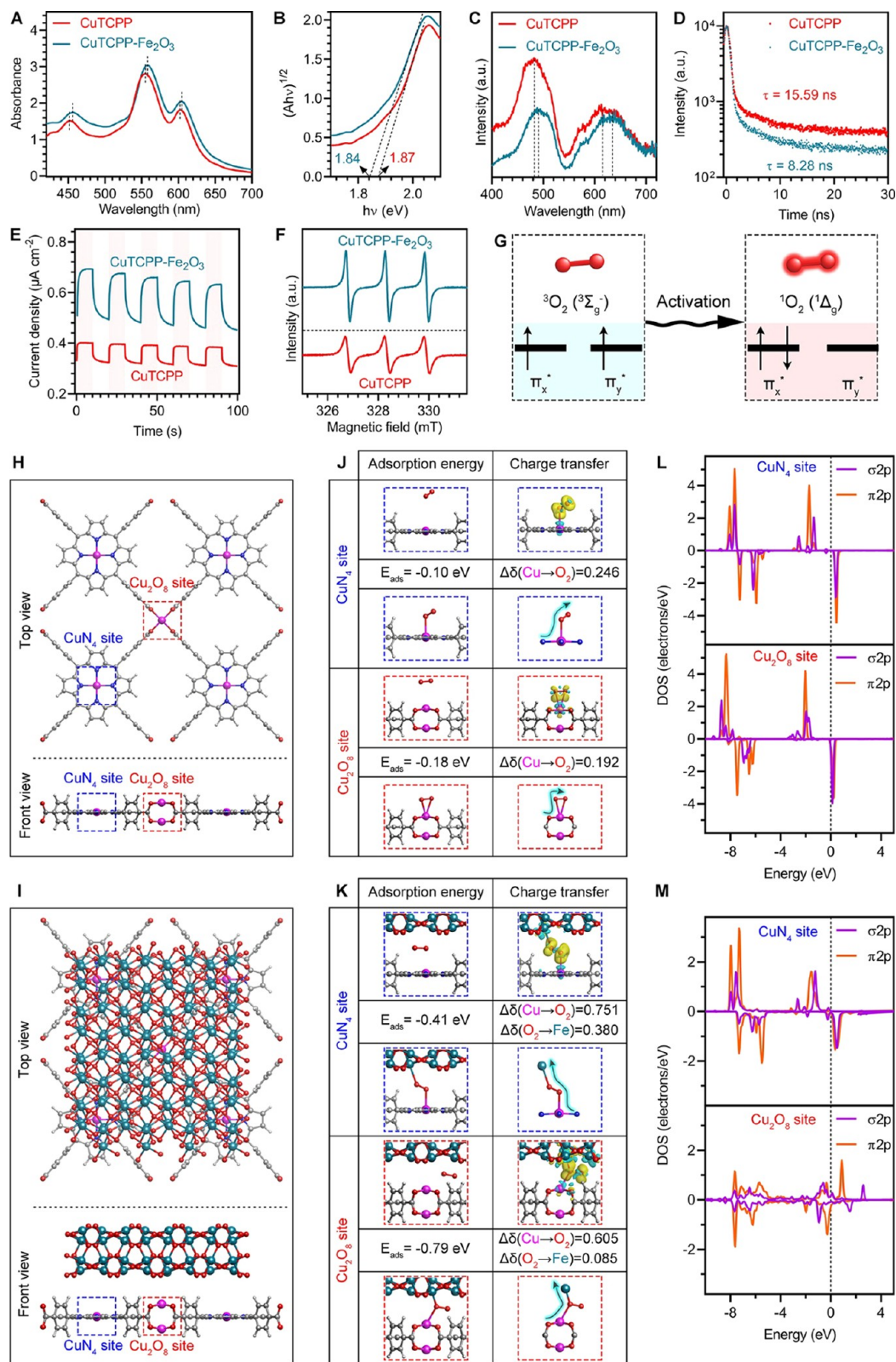
Figure 2. Photocatalytic mechanism. (A) UV−vis diffuse reflectance spectra, (B) Plots of $(\alpha h\nu)^{1/2}$ versus photon energy ($h\nu$), (C) PL spectra, and (D) time-resolved PL decay curves. (E) Photocurrent responses of CuTCPP and CuTCPP-Fe$_2$O$_3$. (F) EPR measurements of ^{1}O$_2$ of CuTCPP and CuTCPP-Fe$_2$O$_3$. (G) Scheme of electron spins at the highest occupied molecular orbital (HOMO) of the ground triplet state ($^3\Sigma_g^-$) of ^{3}O$_2$ and excited singlet state ($^1\Delta_g$) of ^{1}O$_2$. Crystalline structures and corresponding active sites (CuN$_4$ site and Cu$_2$O$_8$ site) of (H) CuTCPP and (I) CuTCPP-Fe$_2$O$_3$ from the top view and front view, respectively. O$_2$ adsorption energies, charge density difference plots of adsorbed O$_2$, and Bader charge calculations of adsorbed O$_2$ on different sites (CuN$_4$ site and Cu$_2$O$_8$ site) in the (J) CuTCPP model and (K) CuTCPP-Fe$_2$O$_3$ model, respectively. pDOS diagrams of adsorbed O$_2$ on different sites (CuN$_4$ site and Cu$_2$O$_8$ site) in the (L) CuTCPP model and (M) CuTCPP-Fe$_2$O$_3$ model, respectively. Atomic color coding in the crystal structure: C, dark gray; N, blue; O, red; H, light gray; Cu, violet; and Fe, deep cyan.

C=C stretching vibrations in the aromatic ring, respectively. The peaks at 1400 and 1000 cm^{-1} corresponded to C−H and C−O stretching vibrations, respectively. Variable-temperature diffuse reflection infrared Fourier transform spectroscopy (VT-DRIFTS) was used to confirm if the synthetic powders of CuTCPP MOFs contained water molecules. In Figure S3, the VT-DRIFTS result of CuTCPP exhibited that the broad peaks near 3500 cm^{-1} arose from overlapping O−H stretching vibrations associated with H−O−H groups (water molecules) and hydroxyl groups (carboxyl groups from TCPP linkers were not chelated with metal nodes on the edge of CuTCPP nanosheets). As the temperature rose from 25 °C to 180 °C in a vacuum, the peak intensity of H−O−H groups did not obviously change, indicating that there was no significant content of water in synthetic CuTCPP powders. A small amount of water might come from air because the synthetic and drying processes involved anhydrous organic solvents. Additionally, in Figure S4, the thermogravimetric analysis (TGA) demonstrated that the curve of the synthetic CuTCPP powders kept in air had no significant difference from that in vacuum at 160 °C before the test, also suggesting that there was no significant content of water in synthetic CuTCPP powders. Therefore, the synthetic powders of CuTCPP MOFs contained no significant content of water because the synthetic and drying processes involved no hydrosolvent.

As shown in Figure 1K, the pore-size distribution curves of CuTCPP and CuTCPP-Fe$_2$O$_3$ demonstrated a similar micropore distribution with an average size of 1.34 and 1.19 nm, respectively. These results were consistent with an interplanar distance of 1.19 nm based on the theoretical crystallographic structure (inset image in Figure 1K). Obviously, after the deposition of Fe$_2$O$_3$, the corresponding micropore decreased from 1.34 nm to 1.19 nm, suggesting that the atomic-layer Fe$_2$O$_3$ was uniformly deposited on CuTCPP to generate a uniform micropore distribution.

Besides, the X-ray photoelectron spectroscopy (XPS) survey spectra (Figure 1L) demonstrated that the four elements (C, N, O, Cu) existed in CuTCPP and CuTCPP-Fe$_2$O$_3$, and CuTCPP-Fe$_2$O$_3$ contained the Fe element. The corresponding characteristic peaks were marked by gray rectangles. Concretely, the elemental contents (atomic percent) of CuTCPP included C 1s (78.92%), N 1s (5.88%), O 1s (12.15%), and Cu 2p (3.05%). The elemental contents of CuTCPP-Fe$_2$O$_3$ comprised C 1s (75.11%), N 1s (5.43%), O 1s (14.29%), Cu 2p (2.25%), and Fe 2p (2.91%). Comparatively, these results fully verified the successful loading of Fe$_2$O$_3$ on CuTCPP. In order to carefully investigate the chemical bonding route and interfacial interaction, the elemental peaks were analyzed and compared. First, the C 1s peaks (Figure S5A) of CuTCPP and CuTCPP-Fe$_2$O$_3$ were calibrated to 284.8 eV and fitted to four subpeaks belonging to C=C (284.8 and 284.8 eV), C−C/C−H (286.0 and 286.1 eV), C−N/C−O (288.3 and 288.3 eV), and C=N/C=O (291.1 and 290.7 eV).[32] In Figure 1M, the N 1s signals were assigned to three subpeaks corresponding to C=N (398.7 eV), C−N (400.0 eV), and pyrrolic N groups,[32,33] where the peak of the pyrrolic N group of CuTCPP-Fe$_2$O$_3$ shifted to lower binding energy from 401.4 eV to 400.1 eV, compared with that of CuTCPP. Meanwhile, in Figure 1N, the O 1s region of the CuTCPP contained C=O (531.8 eV) and C−O (532.6 eV) groups, and the O 1s region of the CuTCPP-Fe$_2$O$_3$ included Fe−O (530.1 eV), C=O (531.8 eV), and C−O (532.2 eV) groups.[32,34] Similarly, the peak of the C−O group of CuTCPP-Fe$_2$O$_3$ had a lower

binding energy than that of CuTCPP. Therefore, the peak shift of the pyrrolic N and C−O group indicated the formation of a tight heterointerface between CuTCPP and Fe$_2$O$_3$. Besides, the Fe 2p peak (Figure S5B) of CuTCPP-Fe$_2$O$_3$ was ascribed to Fe 2p$_{3/2}$ (711.2 and 724.2 eV), Fe 2p$_{1/2}$ (714.5 and 726.2 eV), and satellite (717.7 eV).[35] This binding energy of Fe 2p (Figure S5B) was in good agreement with those of α-Fe$_2$O$_3$ in previous literature.[35] The Cu 2p peaks of CuTCPP and CuTCPP-Fe$_2$O$_3$ are shown in Figure S5C. In summary, the chemical bonding details of CuTCPP and CuTCPP-Fe$_2$O$_3$ were definite and the interfacial interaction between CuTCPP and Fe$_2$O$_3$ is schematically illustrated in Figure S5D. In the CuTCPP-Fe$_2$O$_3$ heterointerface (in Figure S5D), the distance (0.325 nm) between CuTCPP and Fe$_2$O$_3$ was marked and the interaction between Fe$_2$O$_3$ and CuTCPP was due to van der Waals force.

Photocatalytic Performances. The UV−vis diffuse reflectance spectra (Figure 2A) exhibited the optical absorbance of CuTCPP and CuTCPP-Fe$_2$O$_3$ in the range of visible light (400−700 nm). Obviously, CuTCPP-Fe$_2$O$_3$ exhibited three stronger characteristic peaks than CuTCPP, and these characteristic peaks resulted from the photophysical performance of the porphyrinic structure of CuTCPP MOF linkers (TCPP).[14,33] Besides, the certain peak red-shift of CuTCPP-Fe$_2$O$_3$ indicated that the interfacial interaction between CuTCPP and Fe$_2$O$_3$ promoted the optical performance of CuTCPP.[33] Especially, the absorbance signal at 660 nm of CuTCPP-Fe$_2$O$_3$ was enhanced, compared with CuTCPP. Therefore, the CuTCPP-Fe$_2$O$_3$ was expected to be an effective photocatalyst. According to the UV−vis diffuse reflectance spectra (Figure 2A), the calculated plots (Figure 2B) based on Kubelka−Munk function versus bandgap energy demonstrated that CuTCPP and CuTCPP-Fe$_2$O$_3$ had bandgaps of 1.87 and 1.84 eV, respectively.[36] Notably, the photogenerated electron−hole pairs could be separated across the bandgap (1.87 and 1.84 eV) to generate ROS when the excitation wavelength was less than 663.1 nm. Thus, a 660 nm laser could be used as the light source to conduct an effective photocatalytic process. CuTCPP-Fe$_2$O$_3$, with a narrower bandgap, might be a more efficient visible-light-responsive photocatalyst than CuTCPP.

As shown in Figure 2C, the photoluminescence (PL) spectra of CuTCPP and CuTCPP-Fe$_2$O$_3$ revealed two peaks corresponding to ~490 and ~630 nm, respectively. The high PL signal of CuTCPP indicated a relatively quick recombination rate of photogenerated electron−hole pairs, whereas the low PL signal of CuTCPP-Fe$_2$O$_3$ indicated an efficient reduction of radiative recombination of photogenerated electron−hole pairs. Notably, the two PL peaks of CuTCPP-Fe$_2$O$_3$ had an obvious red-shift, suggesting that the electronic states of CuTCPP were hybridized with those of Fe$_2$O$_3$.[37] In summary, the heterointerface of CuTCPP-Fe$_2$O$_3$ was central to the efficient separation of photoexcited electron−hole pairs across the interface, thus prolonging the lifetime of the charge carrier and improving photocatalytic activity. Besides, the time-resolved PL decay curves (Figure 2D) exhibited that the fluorescence lifetime of CuTCPP-Fe$_2$O$_3$ (8.28 ns) was significantly shorter than that of CuTCPP (15.59 ns). After atomic-layer Fe$_2$O$_3$ deposition, the shorter fluorescence lifetime represented the higher charge separation efficiency because the trapping of photogenerated carriers in specific trap sites of CuTCPP-Fe$_2$O$_3$ could cause fast fluorescence decay.

In Figure 2E, the transient photocurrent response under 660 nm laser irradiation was measured by the photoelectrochemical method. The photocurrent intensity of CuTCPP was clearly weaker than that of CuTCPP-Fe_2O_3 in five repeated on/off cycles, also demonstrating the more effective charge transfer in the 2D MOF−Fe_2O_3 heterointerface under 660 nm light irradiation. Meanwhile, electron paramagnetic resonance (EPR) was used to detect ROS production, where 2,2,6,6-tetramethylpiperidine (TEMP) was used as a singlet oxygen probe. In Figure 2F, the characteristic signal (1:1:1) of $^1O_2$ illustrated that the ROS yield of CuTCPP-Fe_2O_3 was higher than that of CuTCPP under 660 nm light irradiation. Therefore, CuTCPP-Fe_2O_3 had a greater advantage and potential than CuTCPP in PDT. Besides the EPR measurements, the 1,3-diphenylisobenzofuran (DPBF) probe was also used to detect the $^1O_2$ production efficiency. As shown in Figure S6, CuTCPP-Fe_2O_3 (Figure S6B) had a greater ability of time-dependent $^1O_2$ generation than CuTCPP (Figure S6A and C), which was consistent with the EPR result (Figure 2F). Notably, the singlet oxygen generation efficiency of CuTCPP MOFs was higher than that of CuTCPP molecules (Figure S7), preliminarily suggesting that the network structure of MOFs had a potential advantage in $^1O_2$ generation due to energy and charge transfer in MOFs. The related mechanism will be discussed below.

Theoretical Calculations. To study the possible binding site of Fe precursors on CuTCPP in the ALD process, an iron *tert*-butoxide molecule was separately adsorbed on the different sites of CuTCPP and the corresponding adsorption energies were calculated (Figure S8). Comparatively, the adsorption energy (−0.41 eV) of the Cu_2O_8 site (Figure S8A) was lower than that (−0.23 eV) of the CuN_4 site (Figure S8B), indicating that the optimized binding site of Fe precursors on CuTCPP in the ALD process was Cu_2O_8 sites. To comprehensively explore the photodynamic mechanism of CuTCPP and CuTCPP-Fe_2O_3, theoretical calculations based on a potential-energy-based model were performed. First, the adsorption and catalytic conversion of molecular oxygen (O_2) on the specific active sites of CuTCPP and CuTCPP-Fe_2O_3 were evaluated by density functional theory (DFT) calculations. As shown in Figure 2G, the electron spins at the highest occupied molecular orbital (HOMO) indicated that the ground triplet state ($^3\sum_g^-$) of $^3O_2$ had two unpaired electrons on individual antibonding π orbitals (π_x^* and π_y^*) and the excited singlet state ($^1\Delta_g$) of $^1O_2$ had paired electrons on an antibonding π orbital (π_x^*).[38] Generally, the catalytic conversion from ground $^3O_2$ to reactive $^1O_2$ could be achieved by energy evolution and charge transfer from the excited state of photosensitizers upon light irradiation.[38] Overall, the catalytic process constituted two steps, i.e., free $^3O_2$ adsorption and adsorbed $^3O_2$ activation into $^1O_2$.[39,40] The corresponding potential energies included adsorption energy (E_{ads}) and activation energy barrier.[39,40]

To investigate the O_2 binding site on CuTCPP and CuTCPP-Fe_2O_3, an O_2 molecule was separately adsorbed on different sites (the CuN_4 site and Cu_2O_8 site) of CuTCPP and CuTCPP-Fe_2O_3 in Figure 2H and I. Overall, the corresponding adsorption energies of the CuTCPP model (Figure 2J) were higher than those of the CuTCPP-Fe_2O_3, model (Figure 2K), suggesting that free $^3O_2$ was more easily adsorbed on CuTCPP-Fe_2O_3. Besides, the adsorption energies (−0.10 eV of CuTCPP and −0.41 eV of CuTCPP-Fe_2O_3) of CuN_4 sites were higher than those (−0.18 eV of CuTCPP and −0.79 eV

of CuTCPP-Fe_2O_3) of Cu_2O_8 sites, thus demonstrating that the optimized O_2 binding site in CuTCPP and CuTCPP-Fe_2O_3 was the Cu_2O_8 sites for the process of free $^3O_2$ adsorption. This spontaneous chemisorption without an energy barrier was beneficial for subsequent catalytic conversion. Notably, in an actual situation in air or in water, besides O_2 molecules, water molecules might also be adsorbed on the Cu_2O_8 sites. Therefore, the CuN_4 sites of CuTCPP and CuTCPP-Fe_2O_3 also needed to be considered, even if its adsorption energy was relatively large.

As shown in Figure 2J and K, during the chemisorption, the charge density difference plots and Bader charge calculations of $^3O_2$ revealed the significant charge transfer between adsorption sites and adsorbed $^3O_2$ in the CuTCPP and CuTCPP-Fe_2O_3 models. Concretely, in the CuTCPP model (Figure 2J), the charge density difference and Bader charge calculation indicated that the electron transfer direction was from the Cu atom to the adsorbed O adatoms due to the forming of Cu−O (adatom) bonding. Further, the electron transfer amount in the CuN_4 site (0.246 electron charge from the Cu atom to O_2 adatoms) was more than that in the Cu_2O_8 site (0.192 electron charge from the Cu atom to O_2 adatoms). Comparatively, in the CuTCPP-Fe_2O_3 model (Figure 2K), the distinct charge distribution on the $^3O_2$ molecule in the CuTCPP-Fe_2O_3 model demonstrated the electron transfer between Cu or Fe atom and adsorbed O adatoms due to the forming of Cu−O (adatom) bonding and Fe−O (adatom) bonding. Correspondingly, the net electron transfer amount of O_2 adatoms (0.371 electron charge) in the CuN_4 site (0.751 electron charge from the Cu atom to O_2 adatoms; 0.380 electron charge from O_2 adatoms to the Fe atom) was less than that of O_2 adatoms (0.520 electron charge) in the Cu_2O_8 site (0.605 electron charge from the Cu atom to O_2 adatoms; 0.085 electron charge from O_2 adatoms to the Fe atom). Overall, the charge transfer amounts between adsorption sites and adsorbed O_2 in the CuTCPP-Fe_2O_3 model were more than those in the CuTCPP model.

Additionally, the projected density of states (pDOS) diagrams (Figure 2L and M) exhibited the state of the electronic density of $\sigma2p$ and $\pi2p$ of $^3O_2$. Compared with free $^3O_2$ (Figure S9), the pDOS curves (Figure 2L) of $^3O_2$ (in CuN_4 site and Cu_2O_8 site) in the CuTCPP model had a slight change due to the orbital hybrid of O (adatom) with the Cu atom, whereas the pDOS profile (Figure 2M) of $^3O_2$ (in CuN_4 site and Cu_2O_8 site) in the CuTCPP-Fe_2O_3 model had an obvious alteration owing to the orbital hybrid of O (adatom) with Fe and Cu atoms.

In summary, these pathways of adsorption energy evolution and charge transfer represented the primary photodynamic mechanism of CuTCPP and CuTCPP-Fe_2O_3. Specifically, exogenous light-activated CuTCPP and CuTCPP-Fe_2O_3 transfer their excited-state energy and exhibit charge transfer to adsorbed ground-state $^3O_2$ for reactive $^1O_2$ generation. This theoretical simulation could be used to explain the experimental results (Figure 2F). Consequently, this mechanism provided an atomistic-level insight into molecular oxygen activation of photodynamic activity. Meanwhile, the theoretical calculations inspired the rational design and catalytic role of 2D MOF-based nanomaterials, including heterostructures.

Ion Release Behavior. The cumulative Cu^{2+} release curves of CuTCPP and CuTCPP-Fe_2O_3 at 37 °C in PBS for short-term release (24 h) and long-term release (28 days) are shown in Figure 3A. Overall, the Cu^{2+} release of CuTCPP and
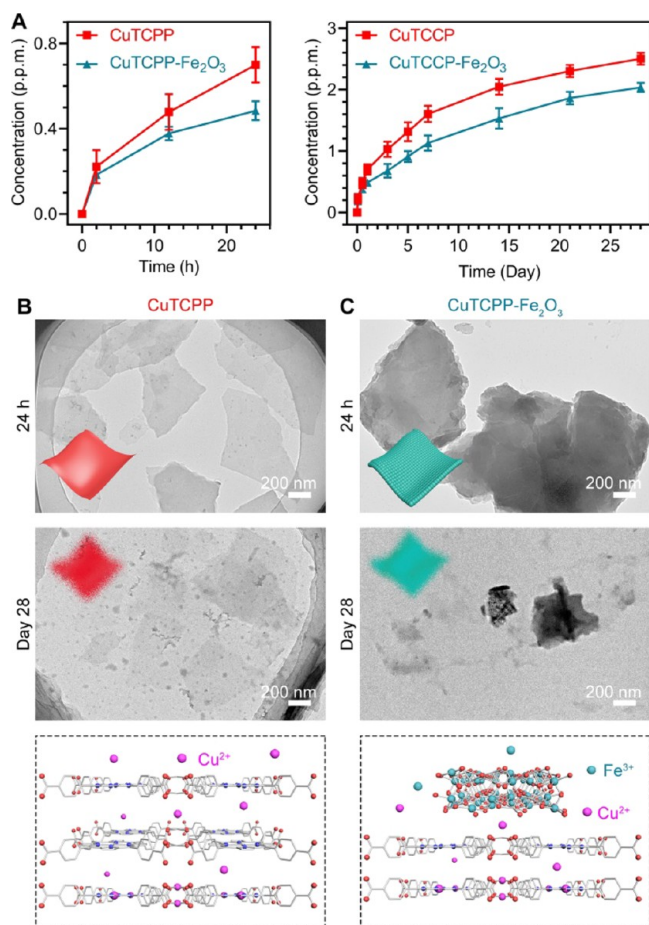
Figure 3. Ion release behavior. (A) Cumulative Cu^{2+} release curves of CuTCPP and CuTCPP-Fe_2O_3 at 37 °C in PBS for short-term release (24 h) and long-term release (28 days), respectively. TEM images of (B) CuTCPP and (C) CuTCPP-Fe_2O_3 immersed in PBS for 24 h and 28 days, respectively. Corresponding schematic illustration of biodegradability of CuTCPP and CuTCPP-Fe_2O_3. Error bars indicate means ± standard deviations (n = 3 independent samples). Atomic color coding in the crystal structure: C, dark gray; N, blue; O, red; Cu, violet; and Fe, deep cyan.

CuTCPP-Fe_2O_3 lasted up to 28 days without any burst release. Moreover, the released Cu^{2+} amount of CuTCPP (200 ppm) was larger than that of CuTCPP-Fe_2O_3 (200 ppm) at the same time point. Concretely, the cumulative Cu^{2+} release of CuTCPP (0.222 ± 0.078 ppm for 2 h and 0.700 ± 0.083 ppm for 24 h) and CuTCPP-Fe_2O_3 (0.184 ± 0.013 ppm for 2 h and 0.485 ± 0.045 ppm for 24 h) within 24 h was relatively quick. Over time, the cumulative Cu^{2+} release of CuTCPP (2.503 ± 0.098 ppm) and CuTCPP-Fe_2O_3 (2.037 ± 0.075 ppm) within 28 days was stable and slow. Additionally, the cumulative Fe^{3+} release curves (Figure S10) of CuTCPP-Fe_2O_3 exhibited a similar trend to Cu^{2+} release curves within 28 days, but the cumulative amouns of Fe^{3+} release for 2 h (0.049 ± 0.012 ppm), 24 h (0.145 ± 0.018 ppm), and 28 days (0.499 ± 0.015 ppm) were far less than that of Cu^{2+} release in the same time, suggesting that Fe_2O_3 had a relatively slower biodegradation than CuTCPP. Besides, the XRD spectra (Figure S11) of CuTCPP immersed in PBS for 1, 3, and 7 days had no significant changes over time, demonstrating that the MOF structure of CuTCPP had no obvious alteration in PBS in a relatively short time (7 days).

To investigate the specific ratio of each component in CuTCPP-Fe_2O_3, the crystal structure in 200 ppm of CuTCPP-Fe_2O_3 solution was completely degraded into metal ions by concentrated nitric acid solution. As shown in Figure S12, the corresponding concentrations of Cu^{2+} and Fe^{3+} were 16.201 ± 0.284 and 4.194 ± 0.158 ppm, respectively. This Fe/Cu mass ratio (0.259) could be used to calculate the Fe/Cu molar ratio (0.294) in CuTCPP-Fe_2O_3. Additionally, in comparison, the cumulative released amounts of Cu^{2+} (2.037 ± 0.075 ppm) and Fe^{3+} (0.499 ± 0.015 ppm) from 200 ppm of CuTCPP-Fe_2O_3 solution in PBS for 28 days were obviously lower than those of total degradation. The low degree of degradation leaching (12.57% Cu^{2+} and 11.90% Fe^{3+}) revealed that CuTCPP-Fe_2O_3 solution in PBS for 28 days demonstrated slight degradation and relative stability.

Further, the TEM images (Figure 3B and C) of CuTCPP and CuTCPP-Fe_2O_3 immersed in PBS for 24 h and 28 days indicated the morphology evolution over time. The morphology of CuTCPP and CuTCPP-Fe_2O_3 had no significant alteration in PBS for 24 h when compared with those in Figure 1C and F. After 28 days, the obvious morphology changes of CuTCPP and CuTCPP-Fe_2O_3 could be found by the residual products after partial degradation. The results demonstrated that the unique biodegradable behavior of CuTCPP and CuTCPP-Fe_2O_3 was determined by their structures during relatively long-term immersion in PBS, which was accompanied by the specific trend of Cu^{2+} release. That is, the two-dimensional porous structures of CuTCPP and CuTCPP-Fe_2O_3 possessed large specific surface areas, acting as carriers to load lots of metal ions (Cu^{2+} and Fe^{3+}). When immersion in PBS, the superficial structures contacted with PBS would be gradually degraded into free metal ions. Over time, the MOF heterojunction-based structures would further collapse, resulting in the obvious changes of degradable morphology after 28 days in PBS. The corresponding biodegradability process of CuTCPP and CuTCPP-Fe_2O_3 is schematically illustrated in Figure 3B and C, where Cu^{2+} and Fe^{3+} were gradually released from the two-dimensional porous structures to generate the fragmentary products. To sum up, the proper biodegradability characteristics of CuTCPP and CuTCPP-Fe_2O_3 were rapid ion release in the short-term and stable ion release in the long-term, showing great potential in antibacterial and bioactive applications.

Antibacterial Mechanism of Photodynamic Ion Therapy. Based on the results of photocatalytic performance and ion release behaviors, the antibacterial experiments were performed by the synergetic effect of photodynamic and ion therapy. Overall, compared with the control groups, CuTCPP and CuTCPP-Fe_2O_3 exhibited effective antimicrobial activities against *P. gingivalis*, *F. nucleatum*, and *S. aureus* under 660 nm light illumination for 20 min, followed by incubation in the dark for 2 h. Specifically, in Figure 4A−C, the CuTCPP group had moderate antibacterial rates of 88.03 ± 5.49% against *P. gingivalis*, 85.51 ± 1.78% against *F. nucleatum*, and 80.31 ± 1.86% against *S. aureus*, respectively. Comparatively, the CuTCPP-Fe_2O_3 group showed higher bacterial-killing efficiency against *P. gingivalis* (99.87 ± 0.09%), *F. nucleatum* (99.57 ± 0.21%), and *S. aureus* (99.03 ± 0.24%).

As shown in Figure S13, in order to explore the synergistic effect of ROS and released ions, the conditions under light for 20 min and in the dark for 2 h at 37 °C were separately performed for comparison. The groups under 660 nm light illumination showed relatively low antibacterial rates against *P.*
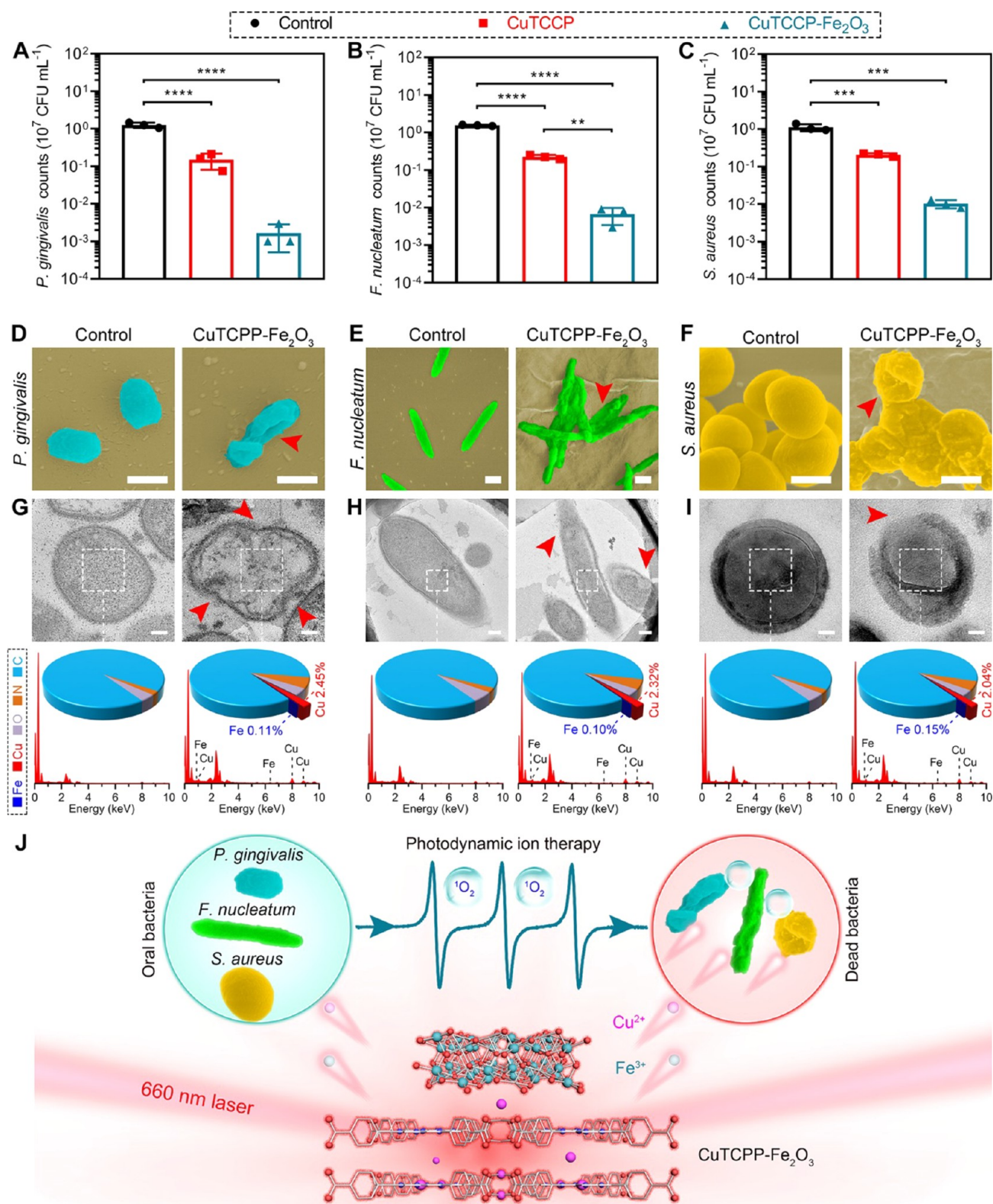
Figure 4. Antibacterial mechanism of photodynamic ion therapy. Viabilities of (A) *P. gingivalis*, (B) *F. nucleatum*, and (C) *S. aureus* treated with CuTCPP and CuTCPP-Fe$_2$O$_3$ under 660 nm laser illumination for 20 min, followed by incubation in the dark for 2 h. SEM images (scale bars = 500 nm for all images) of (D) *P. gingivalis*, (E) *F. nucleatum*, and (F) *S. aureus* treated with CuTCPP-Fe$_2$O$_3$ under 660 nm light illumination for 20 min, followed by incubation in the dark for 2 h. TEM images and corresponding EDS curves of (G) *P. gingivalis* (scale bars = 100 nm), (H) *F. nucleatum* (scale bars = 200 nm), and (I) *S. aureus* (scale bars = 100 nm) treated with CuTCPP-Fe$_2$O$_3$ under 660 nm laser illumination for 20 min, followed by incubation in the dark for 2 h. (J) Scheme of the antibacterial mechanism of photodynamic ion therapy by the synergistic effect of ROS and released ions. Red arrows show obvious damage and deformation of bacteria. Individual data points (*n* = 3 biologically independent samples) and error bars indicate means ± standard deviations. Statistical differences were analyzed by one-way ANOVA and post hoc Tukey's test (****P < 0.0001).
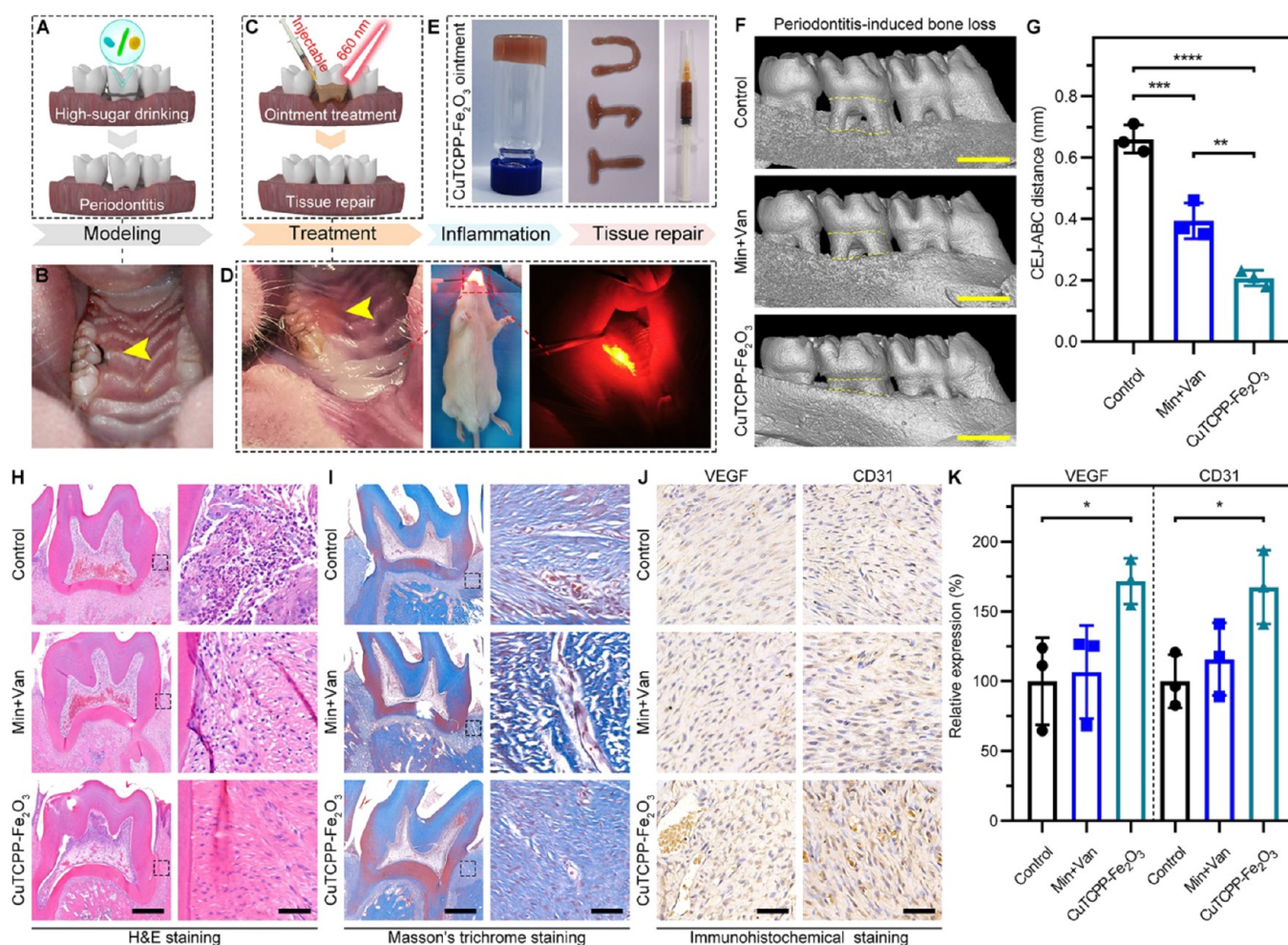
Figure 5. Periodontitis treatment. (A) Schematic illustration of periodontitis modeling. (B) Photographs of silk suture fixing on the second molar during periodontitis modeling. (C) Schematic illustration of periodontitis treatment. (D) Photographs of periodontitis treatment by the injectable CuTCPP-Fe$_2$O$_3$ ointment, followed by illumination of a 660 nm laser for 20 min. (E) Photographs of the injectable CuTCPP-Fe$_2$O$_3$ ointment. (F) 3D reconstructions of the maxillary molar area by micro-CT (scale bars = 1 mm) in three groups (control, Min+Van, and CuTCPP-Fe$_2$O$_3$). Yellow dotted lines mark the distance between CEJ and ABC to reflect the alveolar bone loss. (G) Quantitative measurement of CEJ−ABC distance. Periodontium histological sections by (H) H&E staining and (I) Masson's trichrome staining (scale bars = 500 and 50 μm for low-magnification and high-magnification images, respectively) in three groups (control, Min+Van, and CuTCPP-Fe$_2$O$_3$). Periodontium histological sections by (J) immunohistochemical staining (scale bars = 50 μm for all images) and (K) corresponding quantitative analysis of VEGF and CD31 in the three groups (control, Min+Van, and CuTCPP-Fe$_2$O$_3$). Individual data points (n = 3 biologically independent samples) and error bars indicate means ± standard deviations. Statistical differences were analyzed by one-way ANOVA and post hoc Tukey's test (*P < 0.05, **P < 0.01, ***P < 0.001, ****P < 0.0001).

gingivalis (78.89 ± 1.26% for CuTCPP and 93.09 ± 0.66% for CuTCPP-Fe$_2$O$_3$ in Figure S13A), *F. nucleatum* (77.78 ± 1.12% for CuTCPP and 92.62 ± 0.63% for CuTCPP-Fe$_2$O$_3$ in Figure S13B), and *S. aureus* (72.43 ± 1.29% for CuTCPP and 90.39 ± 1.05% for CuTCPP-Fe$_2$O$_3$ in Figure S13C). Besides, the groups in the dark for 2 h exhibited poor antimicrobial efficiency (less than 45% in all groups in Figure S13D−F). Therefore, the antibacterial effects of synergetic groups (under 660 nm light illumination for 20 min, followed by incubation in the dark for 2 h) were higher than those of the separate groups (under 660 nm light illumination for 20 min or incubation in the dark for 2 h). The greater bactericidal efficiency can be ascribed to the synergistic effect of ROS and released ions.

Notably, the relatively low antibacterial rates of the CuTCPP MOFs under 660 nm light illumination for 20 min indicated that the CuTCPP MOFs were not an excellent photosensitizer for singlet oxygen generation. Except for the

strategy of surface engineering of Fe$_2$O$_3$ by ALD to improve the photodynamic antibacterial activity of CuTCPP MOFs, the alternative metal nodes in MOFs (such as ZnTCPP MOFs) to replace Cu-based nodes may further promote its photocatalytic activity. Therefore, further research on optimized 2D porphyrinic MOFs also has great potential in biomedical applications.

As shown in Figure 4D to F, the three kinds of bacteria (*P. gingivalis*, *F. nucleatum*, and *S. aureus*) after treatment without (the control) and with CuTCPP-Fe$_2$O$_3$ (under 660 nm light illumination for 20 min, followed by incubation in the dark for 2 h) were observed by SEM. *P. gingivalis* in the control group had an intact short rod-like shape (Figure 4D), whereas the morphology of *P. gingivalis* in the CuTCPP-Fe$_2$O$_3$ group showed severe shrinkage and deformation (marked by the red arrow). For *F. nucleatum*, the bacteria had a long-strip shape with an integrated membrane in the control group (Figure 4E), but a corrugated morphology (marked by the red arrow) in the

CuTCPP-Fe$_2$O$_3$ group. Similarly, the morphology of *S. aureus* was spherical and unbroken (Figure 4F), but irregular and distorted (marked by red arrow) in the CuTCPP-Fe$_2$O$_3$ group. To sum up, CuTCPP-Fe$_2$O$_3$ through photodynamic ion therapy against three kinds of bacteria could seriously destroy bacterial membranes, thus resulting in broad-spectrum antimicrobial activity.

To explore whether the released ions (Cu^{2+} and Fe^{3+}) enter the bacteria, the bacteria treated with CuTCPP-Fe$_2$O$_3$ were detected by TEM and EDS. In Figure 4G, the *P. gingivalis* bacteria had a normal morphology with intact bacterial membranes, and the corresponding EDS detection exhibited no Cu and Fe signals in the bacteria. In contrast, the membranes of *P. gingivalis* in the CuTCPP-Fe$_2$O$_3$ group were severely damaged (marked by the red arrow) and showed obvious signals of Cu and Fe. Similarly, *F. nucleatum* (Figure 4H) and *S. aureus* (Figure 4I) in the CuTCPP-Fe$_2$O$_3$ group had a broken morphology and contained certain Cu and Fe elements when compared with the control group. Therefore, the results fully verified that the released ions (Cu^{2+} and Fe^{3+}) in the CuTCPP-Fe$_2$O$_3$ group entered the bacteria, causing effective lethality.

To sum up, the corresponding antibacterial mechanism of photodynamic ion therapy for broad-spectrum bactericidal action is schematically illustrated in Figure 4J. First, the ROS (^{1}O$_2$) produced rapidly under 660 nm light irradiation would destroy the bacterial membrane and increase its permeability. Meanwhile, the released ions (Cu^{2+} and Fe^{3+}) would rapidly penetrate the damaged bacterial membrane and enter the bacteria, leading to bacterial metabolic disorders. The synergy of ROS and released ions brought more insight into a broad-spectrum antibacterial strategy and has great potential in periodontitis treatment.

Cytocompatibility Evaluation. The cell viabilities in different groups are shown in Figure S14. Overall, the CuTCPP-Fe$_2$O$_3$ group exhibited better cytocompatibility than the CuTCPP group in the dark. Specifically, in Figure S14A, the cell viabilities of CuTCPP and CuTCPP-Fe$_2$O$_3$ were 87.07 ± 6.72% and 95.98 ± 9.02% on day 1, respectively. The relatively poor cytocompatibility on day 1 was ascribed to the rapid release of metal ions. Over time, the cytocompatibility in CuTCPP and CuTCPP-Fe$_2$O$_3$ groups gradually improved. Especially on day 7, the cell viabilities of CuTCPP (101.64 ± 4.06%) and CuTCPP-Fe$_2$O$_3$ (116.98 ± 3.87%) were highest when compared with those on day 1 and day 3. Notably, CuTCPP-Fe$_2$O$_3$ could promote cell proliferation over time, resulting from the proper biodegradability and slow ion release of CuTCPP-Fe$_2$O$_3$ in the relatively long-term (Figure 3). Correspondingly, under 660 nm laser irradiation for 20 min (Figure S14B), the cell viabilities of the CuTCPP and CuTCPP-Fe$_2$O$_3$ groups had a similar tendency to those in the dark over time. However, the definite cytotoxicity of CuTCPP (58.39 ± 2.37%) and CuTCPP-Fe$_2$O$_3$ (58.85 ± 2.51%) on day 1 demonstrated that the generated ROS had an adverse impact on cells. Over time, the cytotoxicity induced by ROS was significantly relieved. Moreover, the cell viabilities of CuTCPP (100.51 ± 4.13%) and CuTCPP-Fe$_2$O$_3$ (111.59 ± 3.26%) on day 7 were close to those in the dark, suggesting that the adverse influence of ROS gradually decreased over time.

Actually, tetrakis(4-carboxyphenyl)porphyrin (TCPP) serving as a biocompatible photosensitizer has been widely used in biomedical applications.[14] The whole square geometry of TCPP was rigid, while the terminal phenyl ring of TCPP was rotatable. Therefore, various metal nodes could be connected with TCPP to generate diverse MOFs with different topologies.[16] Among the linkers in porphyrinic MOFs, the carboxylate-based linker (TCPP) was the most common as compared with the other linkers, including tetratopic 5,10,15,20-tetra(1*H*-pyrazol-4-yl)porphyrin (TPP) and *meso*-tetra(*N*-methyl-4-pyridyl)porphine tetratosylate (TMP).[14,16]

Notably, the cytocompatibility of MOFs for biomedical applications should be comprehensively evaluated. For example, Bagherzadeh et al. developed biocompatible MOF-based nanocarriers for drug loading,[19,20] for which comprehensive cytotoxicity studies were performed. In summary, from the biological perspective, the characteristics of excellent cytocompatibility of CuTCPP and CuTCPP-Fe$_2$O$_3$ exhibited great potential in biomaterials (such as periodontitis) because the proper biodegradability avoided the long-term preservation and unpredictable adverse impacts in vivo.[14,17,19,20,27,29] Meanwhile, the released copper ions from biodegradable CuTCPP and CuTCPP-Fe$_2$O$_3$ are bioactive components, featuring specific biological effect in vivo (such as angiogenesis improvement) and certain antibacterial activity.[29]

Periodontitis Treatment. The periodontitis modeling is schematically illustrated in Figure 5A, which consisted of three parts (silk suture fixing, bacterial liquid addition, and high-sugar drinking). The details are described in the Experimental Section. The silk suture fixing (Figure 5B) was performed on the maxillary second molar during the periodontitis modeling. As shown in Figure 5C and D, the periodontitis was treated by injectable CuTCPP-Fe$_2$O$_3$ ointment, followed by illumination of a 660 nm laser for 20 min, and the periodontitis would experience the process of inflammation and tissue repair. As the periodontitis lesion was close to superficial tissue and the 660 nm light source had the ability of certain tissue penetration, the treatment under 660 nm light irradiation (Figure 5D) was appropriate for periodontitis. The injectable CuTCPP-Fe$_2$O$_3$ ointment (Figure 5E) prepared by poly-ethylene glycol (PEG) had definite adhesion, favoring the adhesion of materials at the site of the periodontitis.

To compare the therapeutic effect of CuTCPP-Fe$_2$O$_3$ ointment with clinical antibiotic therapy, minocycline and vancomycin (Min+Van) were selected as the positive control. As shown in Figure 5F, the 3D reconstructions of the maxillary molar area by micro-CT in the three groups (control, Min+Van, and CuTCPP-Fe$_2$O$_3$) after 28 days of treatment were conducted. The corresponding degree of alveolar bone loss was quantitatively evaluated (Figure 5G) by the yellow dotted lines, marking the distance between the cementoenamel junction (CEJ) and the alveolar bone crest (ABC). Obviously, the CuTCPP-Fe$_2$O$_3$ group (0.21 ± 0.03 mm) had a smaller CEJ−ABC distance than the control group (0.66 ± 0.05 mm) and Min+Van group (0.39 ± 0.06 mm). The results fully verified that the therapeutic effect of CuTCPP-Fe$_2$O$_3$ was significantly better than the clinical antibiotic therapy (Min+Van).

In Figure 5H, the periodontium sections stained by hematoxylin and eosin (H&E) indicated the inflammatory responses in the three groups after 7 days of treatment. Concretely, a large number of neutrophils in the control group were observed, exhibiting severe bacterial infection. In contrast, the number of neutrophils in the Min+Van and CuTCPP-Fe$_2$O$_3$ groups was significantly fewer than that in the control group, demonstrating the reduced bacterial infection. More-

over, the CuTCPP-Fe$_2$O$_3$ group had a minimum inflammatory response, suggesting the effective antibacterial ability of CuTCPP-Fe$_2$O$_3$ in vivo.

Besides, the levels of collagen deposition (blue region in Figure 5I) after 28 days of treatment were observed and compared in periodontium histological sections by Masson's trichrome staining. Obviously, the CuTCPP-Fe$_2$O$_3$ group showed higher levels of collagen deposition (blue region) than the control and Min+Van groups, preliminarily suggesting the excellent ability of tissue repair of CuTCPP-Fe$_2$O$_3$ for periodontitis. To explore the mechanism of tissue repair, the specific capability of angiogenesis was evaluated by immunohistochemical staining of vascular endothelial growth factor (VEGF) and CD31 (also named PECAM1) in the three groups.[29,41−43] In Figure 5J and K, the levels of angiogenesis-correlated VEGF and CD31 in the CuTCPP-Fe$_2$O$_3$ group were significantly higher than those in the control and Min+Van groups. The results confirmed the high angiogenic activity of the CuTCPP-Fe$_2$O$_3$ ointment because VEGF acted as an important direct neovascularization factor and CD31 was positive for angiogenic activity. To sum up, the mechanism of tissue repair of CuTCPP-Fe$_2$O$_3$ ointment was that the released Cu^{2+} from CuTCPP-Fe$_2$O$_3$ could promote collagen deposition and angiogenesis, thus accelerating the recruitment and differentiation of periodontium cells during the recovery process of periodontitis.

Figure S15 shows the hematology results of the CuTCPP-Fe$_2$O$_3$ ointment within the corresponding normal scope (marked by dashed lines), including hematocrit (HCT), hemoglobin (HGB), mean corpuscular hemoglobin (MCH), mean corpuscular hemoglobin concentration (MCHC), mean corpuscular volume (MCV), mean platelet volume (MPV), platelet count (PLT), red blood cell count (RBC), red cell distribution width (RDW), and white blood cell count (WBC). Besides, as shown in Figure S16, the histological analyses of major organs (heart, liver, spleen, lung, and kidney) by H&E staining after 28 days of treatment indicated that the CuTCPP-Fe$_2$O$_3$ ointment had good biosafety in vivo, showing no significant differences between the healthy control and the CuTCPP-Fe$_2$O$_3$ group (no sign of organ damage). Notably, the summary and comparison of MOF's biomedical application and periodontitis therapies with different materials and therapeutic strategies are listed in Table S1. Comparatively, the therapeutic strategy of photodynamic ion therapy in this work had relatively more advantages, including antibacterial activity, alleviative inflammation, and improved angiogenesis to accelerate tissue repair. Therefore, this multifunctional nanomaterial preliminarily exhibited a certain potential in clinical applications of periodontitis treatment and biomedical applications.[44−48]

CONCLUSIONS

CuTCPP-Fe$_2$O$_3$ ointment is prepared by atomic-layer Fe$_2$O$_3$ deposition on porphyrinic MOF (CuTCPP) nanosheets to obtain a CuTCPP-Fe$_2$O$_3$ heterojunction, further forming the ointment by a polyethylene glycol matrix. The theoretical calculation based on an energy evolution pathway and charge transfer identifies the photodynamic mechanism of the heterointerface. The enhanced photocatalytic activity of the 2D MOF heterointerface results from the lower adsorption energy and more charge transfer due to the synergistic effect of metal−linker bridging units, abundant active sites, and the excellent light-harvesting network. This biocompatible and biodegradable 2D MOF heterostructure exhibits broad-spectrum antimicrobial activity (>99%) against diverse oral pathogens by the synergistic effect of ROS and released ions. The in vivo results confirm that this photodynamic ion therapy has a greater therapeutic effect than the reported clinical treatment for periodontitis by minocycline and vancomycin due to the reduced inflammation and promoted angiogenesis. This platform may bring further insight and understanding of periodontitis treatment through photodynamic ion therapy.

ASSOCIATED CONTENT

ⓢ Supporting Information

The Supporting Information is available free of charge at https://pubs.acs.org/doi/10.1021/jacs.1c07875.

Experimental section, Figures S1−S16 (HRTEM, FTIR, VT-DRIFTS, TGA, XPS, DPBF, EPR, DFT, ICP, XRD, bacterial viabilities, cell viabilities, hematology, and H&E staining of main organs), and Table S1 (PDF)

AUTHOR INFORMATION

Corresponding Authors

Xiangmei Liu − *Biomedical Materials Engineering Research Center, Collaborative Innovation Center for Advanced Organic Chemical Materials Co-constructed by the Province and Ministry, Hubei Key Laboratory of Polymer Materials, Ministry-of-Education Key Laboratory for the Green Preparation and Application of Functional Materials, School of Materials Science & Engineering, Hubei University, Wuhan 430062, China;* ⓞ orcid.org/0000-0002-6469-2363; Email: liuxiangmei1978@163.com

Xingcai Zhang − *School of Engineering, Massachusetts Institute of Technology, Cambridge, Massachusetts 02139, United States; School of Engineering and Applied Sciences, Harvard University, Cambridge, Massachusetts 02138, United States;* ⓞ orcid.org/0000-0001-7114-1095; Email: xingcai@mit.edu

Shuilin Wu − *School of Materials Science & Engineering, the Key Laboratory of Advanced Ceramics and Machining Technology by the Ministry of Education of China, Tianjin University, Tianjin 300072, China;* Email: shuilinwu@tju.edu.cn

Authors

Jun Li − *School of Materials Science & Engineering, the Key Laboratory of Advanced Ceramics and Machining Technology by the Ministry of Education of China, Tianjin University, Tianjin 300072, China*

Shuang Song − *School of Engineering, Massachusetts Institute of Technology, Cambridge, Massachusetts 02139, United States*

Jiashen Meng − *School of Engineering, Massachusetts Institute of Technology, Cambridge, Massachusetts 02139, United States*

Lei Tan − *Biomedical Materials Engineering Research Center, Collaborative Innovation Center for Advanced Organic Chemical Materials Co-constructed by the Province and Ministry, Hubei Key Laboratory of Polymer Materials, Ministry-of-Education Key Laboratory for the Green Preparation and Application of Functional Materials, School of Materials Science & Engineering, Hubei University, Wuhan 430062, China;* ⓞ orcid.org/0000-0001-7704-9476

Yufeng Zheng − *School of Materials Science & Engineering, State Key Laboratory for Turbulence and Complex System, Peking University, Beijing 100871, China;* orcid.org/0000-0002-7402-9979

Zhaoyang Li − *School of Materials Science & Engineering, the Key Laboratory of Advanced Ceramics and Machining Technology by the Ministry of Education of China, Tianjin University, Tianjin 300072, China*

Kelvin Wai Kwok Yeung − *Department of Orthopaedics & Traumatology, Li Ka Shing Faculty of Medicine, The University of Hong Kong, Hong Kong 999077, China;* orcid.org/0000-0003-0887-088X

Zhenduo Cui − *School of Materials Science & Engineering, the Key Laboratory of Advanced Ceramics and Machining Technology by the Ministry of Education of China, Tianjin University, Tianjin 300072, China*

Yanqin Liang − *School of Materials Science & Engineering, the Key Laboratory of Advanced Ceramics and Machining Technology by the Ministry of Education of China, Tianjin University, Tianjin 300072, China;* orcid.org/0000-0001-6317-8314

Shengli Zhu − *School of Materials Science & Engineering, the Key Laboratory of Advanced Ceramics and Machining Technology by the Ministry of Education of China, Tianjin University, Tianjin 300072, China;* orcid.org/0000-0002-0190-2626

Complete contact information is available at:
https://pubs.acs.org/10.1021/jacs.1c07875

■ ACKNOWLEDGMENTS

■ REFERENCES

(1) Hajishengallis, G.; Chavakis, T. Local and Systemic Mechanisms Linking Periodontal Disease and Inflammatory Comorbidities. *Nat. Rev. Immunol.* **2021**, *21*, 426−440.

(2) Ghassib, I. H.; Batarseh, F. A.; Wang, H.-L.; Borgnakke, W. S. Clustering by Periodontitis-Associated Factors—A Novel Application to NHANES Data. *J. Periodontol.* **2021**, *92*, 1136−1150.

(3) Kim, D.; Barraza, J. P.; Arthur, R. A.; Hara, A.; Lewis, K.; Liu, Y.; Scisci, E. L.; Hajishengallis, E.; Whiteley, M.; Koo, H. Spatial Mapping of Polymicrobial Communities Reveals a Precise Biogeography Associated with Human Dental Caries. *Proc. Natl. Acad. Sci. U. S. A.* **2020**, *117*, 12375−12386.

(4) Freire, M.; Nelson, K. E.; Edlund, A. The Oral Host−Microbial Interactome: an Ecological Chronometer of Health? *Trends Microbiol.* **2021**, *29*, 551−561.

(5) Wu, S.; Xu, J.; Zou, L.; Luo, S.; Yao, R.; Zheng, B.; Liang, G.; Wu, D.; Li, Y. Long-Lasting Renewable Antibacterial Porous Polymeric Coatings Enable Titanium Biomaterials to Prevent and Treat Peri-Implant Infection. *Nat. Commun.* **2021**, *12*, 3303.

(6) Xi, Y.; Wang, Y.; Gao, J.; Xiao, Y.; Du, J. Dual Corona Vesicles with Intrinsic Antibacterial and Enhanced Antibiotic Delivery Capabilities for Effective Treatment of Biofilm-Induced Periodontitis. *ACS Nano* **2019**, *13*, 13645−13657.

(7) Kitamoto, S.; Nagao-Kitamoto, H.; Jiao, Y.; Gillilland, M. G.; Hayashi, A.; Imai, J.; Sugihara, K.; Miyoshi, M.; Brazil, J. C.; Kuffa, P.; Hill, B. D.; Rizvi, S. M.; Wen, F.; Bishu, S.; Inohara, N.; Eaton, K. A.; Nusrat, A.; Lei, Y. L.; Giannobile, W. V.; Kamada, N. The Intermucosal Connection between the Mouth and Gut in Commensal Pathobiont-Driven Colitis. *Cell* **2020**, *182*, 447−462.

(8) Shen, Z.; Kuang, S.; Zhang, Y.; Yang, M.; Qin, W.; Shi, X.; Lin, Z. Chitosan Hydrogel Incorporated with Dental Pulp Stem Cell-Derived Exosomes Alleviates Periodontitis in Mice via a Macrophage-Dependent Mechanism. *Bioact. Mater.* **2020**, *5*, 1113−1126.

(9) Li, X.; Lovell, J. F.; Yoon, J.; Chen, X. Clinical Development and Potential of Photothermal and Photodynamic Therapies for Cancer. *Nat. Rev. Clin. Oncol.* **2020**, *17*, 657−674.

(10) Gao, D.; Guo, X.; Zhang, X.; Chen, S.; Wang, Y.; Chen, T.; Huang, G.; Gao, Y.; Tian, Z.; Yang, Z. Multifunctional Photo-theranostic Nanomedicine for Cancer Imaging and Treatment. *Mater. Today Bio* **2020**, *5*, 100035.

(11) Sun, X.; Sun, J.; Sun, Y.; Li, C.; Fang, J.; Zhang, T.; Wan, Y.; Xu, L.; Zhou, Y.; Wang, L.; Dong, B. Oxygen Self-Sufficient Nanoplatform for Enhanced and Selective Antibacterial Photo-dynamic Therapy against Anaerobe-Induced Periodontal Disease. *Adv. Funct. Mater.* **2021**, *31*, 2101040.

(12) Zhao, X.; Liu, J.; Fan, J.; Chao, H.; Peng, X. Recent Progress in Photosensitizers for Overcoming the Challenges of Photodynamic Therapy: from Molecular Design to Application. *Chem. Soc. Rev.* **2021**, *50*, 4185−4219.

(13) Ren, Y.; Liu, H.; Liu, X.; Zheng, Y.; Li, Z.; Li, C.; Yeung, K. W. K.; Zhu, S.; Liang, Y.; Cui, Z.; Wu, S. Photoresponsive Materials for Antibacterial Applications. *Cell Rep. Phys. Sci.* **2020**, *1*, 100245.

(14) Rabiee, N.; Yaraki, M. T.; Garakani, S. M.; Garakani, S. M.; Ahmadi, S.; Lajevardi, A.; Bagherzadeh, M.; Rabiee, M.; Tayebi, L.; Tahriri, M.; Hamblin, M. R. Recent Advances in Porphyrin-based Nanocomposites for Effective Targeted Imaging and Therapy. *Biomaterials* **2020**, *232*, 119707.

(15) Meng, J.; Li, J.; Liu, J.; Zhang, X.; Jiang, G.; Ma, L.; Hu, Z.-Y.; Xi, S.; Zhao, Y.; Yan, M.; Wang, P.; Liu, X.; Li, Q.; Liu, J. Z.; Wu, T.; Mai, L. Universal Approach to Fabricating Graphene-Supported Single-Atom Catalysts from Doped ZnO Solid Solutions. *ACS Cent. Sci.* **2020**, *6*, 1431−1440.

(16) Feng, L.; Wang, K.-Y.; Joseph, E.; Zhou, H.-C. Catalytic Porphyrin Framework Compounds. *Trends Chem.* **2020**, *2*, 555−568.

(17) Zheng, Q.; Liu, X.; Zheng, Y.; Yeung, K. W. K.; Cui, Z.; Liang, Y.; Li, Z.; Zhu, S.; Wang, X.; Wu, S. The Recent Progress on Metal−Organic Frameworks for Phototherapy. *Chem. Soc. Rev.* **2021**, *50*, 5086−5125.

(18) Meng, J.; Liu, Z.; Liu, X.; Yang, W.; Wang, L.; Li, Y.; Cao, Y.-C.; Zhang, X.; Mai, L. Scalable Fabrication and Active Site Identification of MOF Shell-Derived Nitrogen-Doped Carbon Hollow Frameworks for Oxygen Reduction. *J. Mater. Sci. Technol.* **2021**, *66*, 186−192.

(19) Rabiee, N.; Bagherzadeh, M.; Haris, M. H.; Ghadiri, A. M.; Moghaddam, F. M.; Fatahi, Y.; Dinarvand, R.; Jarahiyan, A.; Ahmadi, S.; Shokouhimehr, M. Polymer-Coated NH_2-UiO-66 for the Codelivery of DOX/pCRISPR. *ACS Appl. Mater. Interfaces* **2021**, *13*, 10796−10811.

(20) Rabiee, N.; Bagherzadeh, M.; Jouyandeh, M.; Zarrintaj, P.; Saeb, M. R.; Mozafari, M.; Shokouhimehr, M.; Varma, R. S. Natural Polymers Decorated MOF-MXene Nanocarriers for Co-delivery of Doxorubicin/pCRISPR. *ACS Appl. Bio Mater.* **2021**, *4*, 5106−5121.

(21) Jiang, Z. W.; Zhao, T. T.; Zhen, S. J.; Li, C. M.; Li, Y. F.; Huang, C. Z. A 2D MOF-Based Artificial Light-Harvesting System with Chloroplast Bionic Structure for Photochemical Catalysis. *J. Mater. Chem. A* **2021**, *9*, 9301−9306.

(22) Hu, W.-C.; Pang, J.; Biswas, S.; Wang, K.; Wang, C.; Xia, X.-H. Ultrasensitive Detection of Bacteria Using a 2D MOF Nanozyme-Amplified Electrochemical Detector. *Anal. Chem.* **2021**, *93*, 8544−8552.

(23) Jiang, S.; Shi, X.; Zu, Y.; Sun, F.; Zhu, G. Interfacial Growth of 2D MOF Membranes via Contra-Diffusion for CO2 Separation. *Mater. Chem. Front.* **2021**, *5*, 5150−5157.

(24) Dhakshinamoorthy, A.; Asiri, A. M.; Garcia, H. 2D Metal−Organic Frameworks as Multifunctional Materials in Heterogeneous Catalysis and Electro/Photocatalysis. *Adv. Mater.* **2019**, *31*, 1900617.

(25) Hu, H.; Wang, Z.; Cao, L.; Zeng, L.; Zhang, C.; Lin, W.; Wang, C. Metal−Organic Frameworks Embedded in a Liposome Facilitate Overall Photocatalytic Water Splitting. *Nat. Chem.* **2021**, *13*, 358−366.

(26) Zhao, Y.; Zhang, L.; Liu, J.; Adair, K.; Zhao, F.; Sun, Y.; Wu, T.; Bi, X.; Amine, K.; Lu, J.; Sun, X. Atomic/Molecular Layer Deposition for Energy Storage and Conversion. *Chem. Soc. Rev.* **2021**, *50*, 3889−3956.

(27) Ji, X.; Ge, L.; Liu, C.; Tang, Z.; Xiao, Y.; Chen, W.; Lei, Z.; Gao, W.; Blake, S.; De, D.; Shi, B.; Zeng, X.; Kong, N.; Zhang, X.; Tao, W. Capturing Functional Two-Dimensional Nanosheets from Sandwich-Structure Vermiculite for Cancer Theranostics. *Nat. Commun.* **2021**, *12*, 1124.

(28) Yang, J.; Zhang, X.; Liu, C.; Wang, Z.; Deng, L.; Feng, C.; Tao, W.; Xu, X.; Cui, W. Biologically Modified Nanoparticles as Theranostic Bionanomaterials. *Prog. Mater. Sci.* **2021**, *118*, 100768.

(29) Dong, C.; Feng, W.; Xu, W.; Yu, L.; Xiang, H.; Chen, Y.; Zhou, J. The Coppery Age: Copper (Cu)-Involved Nanotheranostics. *Adv. Sci.* **2020**, *7*, 2001549.

(30) Zhao, M.; Wang, Y.; Ma, Q.; Huang, Y.; Zhang, X.; Ping, J.; Zhang, Z.; Lu, Q.; Yu, Y.; Xu, H.; Zhao, Y.; Zhang, H. Ultrathin 2D Metal−Organic Framework Nanosheets. *Adv. Mater.* **2015**, *27*, 7372−7378.

(31) Zhao, W.; Peng, J.; Wang, W.; Jin, B.; Chen, T.; Liu, S.; Zhao, Q.; Huang, W. Interlayer Hydrogen-Bonded Metal Porphyrin Frameworks/MXene Hybrid Film with High Capacitance for Flexible All-Solid-State Supercapacitors. *Small* **2019**, *15*, 1901351.

(32) Ang, H.; Hong, L. Polycationic Polymer-Regulated Assembling of 2D MOF Nanosheets for High-Performance Nanofiltration. *ACS Appl. Mater. Interfaces* **2017**, *9*, 28079−28088.

(33) Yang, F.; Hu, W.; Yang, C.; Patrick, M.; Cooksy, A. L.; Zhang, J.; Aguiar, J. A.; Fang, C.; Zhou, Y.; Meng, Y. S.; Huang, J.; Gu, J. Tuning Internal Strain in Metal−Organic Frameworks via Vapor Phase Infiltration for CO2 Reduction. *Angew. Chem., Int. Ed.* **2020**, *59*, 4572−4580.

(34) Khosravi, H. B.; Rahimi, R.; Rabbani, M.; Maleki, A.; Mollahosseini, A. Design, Facile Synthesis and Characterization of Porphyrin-Zirconium-Ferrite@SiO2 Core-Shell and Catalytic Application in Cyclohexane Oxidation. *Silicon* **2021**, *13*, 451−465.

(35) Balan, A. P.; Radhakrishnan, S.; Woellner, C. F.; Sinha, S. K.; Deng, L.; de los Reyes, C.; Rao, B. M.; Paulose, M.; Neupane, R.; Apte, A.; Kochat, V.; Vajtai, R.; Harutyunyan, A. R.; Chu, C.-W.; Costin, G.; Galvao, D. S.; Martí, A. A.; van Aken, P. A.; Varghese, O. K.; Tiwary, C. S.; Iyer, A. M. M. R.; Ajayan, P. M. Exfoliation of a Non-van der Waals Material from Iron Ore Hematite. *Nat. Nanotechnol.* **2018**, *13*, 602−609.

(36) Jiang, Z. W.; Zou, Y. C.; Zhao, T. T.; Zhen, S. J.; Li, Y. F.; Huang, C. Z. Controllable Synthesis of Porphyrin-Based 2D Lanthanide Metal−Organic Frameworks with Thickness- and Metal-Node-Dependent Photocatalytic Performance. *Angew. Chem., Int. Ed.* **2020**, *59*, 3300−3306.

(37) Xu, G.; Zhang, H.; Wei, J.; Zhang, H.-X.; Wu, X.; Li, Y.; Li, C.; Zhang, J.; Ye, J. Integrating the g-C3N4 Nanosheet with B−H Bonding Decorated Metal−Organic Framework for CO2 activation and Photoreduction. *ACS Nano* **2018**, *12*, 5333−5340.

(38) Nosaka, Y.; Nosaka, A. Y. Generation and Detection of Reactive Oxygen Species in Photocatalysis. *Chem. Rev.* **2017**, *117*, 11302−11336.

(39) Shen, X.; Liu, W.; Gao, X.; Lu, Z.; Wu, X.; Gao, X. Mechanisms of Oxidase and Superoxide Dismutation-like Activities of Gold, Silver, Platinum, and Palladium, and Their Alloys: A General Way to the Activation of Molecular Oxygen. *J. Am. Chem. Soc.* **2015**, *137*, 15882−15891.

(40) Long, R.; Mao, K.; Ye, X.; Yan, W.; Huang, Y.; Wang, J.; Fu, Y.; Wang, X.; Wu, X.; Xie, Y.; Xiong, Y. Surface Facet of Palladium Nanocrystals: A Key Parameter to the Activation of Molecular Oxygen for Organic Catalysis and Cancer Treatment. *J. Am. Chem. Soc.* **2013**, *135*, 3200−3207.

(41) Jin, L.; Guo, X.; Gao, D.; Wu, C.; Hu, B.; Tan, G.; Du, N.; Cai, X.; Yang, Z.; Zhang, X. NIR-Responsive Mxene Nanobelts for Wound Healing. *NPG Asia Mater.* **2021**, *13*, 24.

(42) Ouyang, J.; Ji, X.; Zhang, X.; Feng, C.; Tang, Z.; Kong, N.; Xie, A.; Wang, J.; Sui, X.; Deng, L.; Liu, Y.; Kim, J. S.; Cao, Y.; Tao, W. In Situ Sprayed NIR-Responsive, Analgesic Black Phosphorus-Based Gel for Diabetic Ulcer Treatment. *Proc. Natl. Acad. Sci. U. S. A.* **2020**, *117*, 28667−28677.

(43) Qiao, Y.; Ping, Y.; Zhang, H.; Zhou, B.; Liu, F.; Yu, Y.; Xie, T.; Li, W.; Zhong, D.; Zhang, Y.; Yao, K.; Santos, H. A.; Zhou, M. Laser-Activatable CuS Nanodots to Treat Multidrug-Resistant Bacteria and Release Copper Ion to Accelerate Healing of Infected Chronic Nonhealing Wounds. *ACS Appl. Mater. Interfaces* **2019**, *11*, 3809−3822.

(44) Zhou, M.; Zhang, X.; Xie, J.; Qi, R.; Lu, H.; Leporatti, S.; Chen, J.; Hu, Y. pH-sensitive poly(*β*-amino ester)s nanocarriers facilitate the inhibition of drug resistance in breast cancer cells. *Nanomaterials* **2018**, *8*, 952.

(45) Gao, D.; Chen, T.; Han, Y.; Chen, S.; Wang, Y.; Guo, X.; Wang, H.; Chen, X.; Guo, M.; Zhang, Y. S.; Hong, G.; Zhang, X.; Tian, Z.; Yang, Z. Targeting Hypoxic Tumors with Hybrid Nanobullets for Oxygen-independent Synergistic Photothermal-thermodynamic Therapy. *Nano-Micro Lett.* **2021**, *13*, 99.

(46) Kim, W. Y.; Won, M.; Koo, S.; Zhang, X.; Kim, J. S. Mitochondrial H2Sn-Mediated Anti-Inflammatory Theranostics. *Nano-Micro Lett.* **2021**, *13*, 168.

(47) Kong, N.; Zhang, H.; Feng, C.; Liu, C.; Xiao, Y.; Zhang, X.; Mei, L.; Kim, J. S.; Tao, W.; Ji, X. Arsenene-mediated multiple independently targeted reactive oxygen species burst for cancer therapy. *Nat. Commun.* **2021**, *12*, 4777.

(48) Liu, C.; Sun, S.; Feng, Q.; Wu, Y.; Kong, N.; Yu, Z.; Yao, J.; Zhang, X.; Chen, W.; Tang, Z.; Xiao, Y.; Huang, X.; Lv, A.; Cao, Y.; Wu, A.; Xie, T.; Tao, W. Arsenene nanodot with selective killing effects for solid tumor therapy. *Adv. Mater.* **2021**, 2102054.